Received: 29 April 2022 | Revised: 13 September 2022 | Accepted: 14 September 2022

DOI: 10.1002/wnan.1858

ADVANCED REVIEW

WIREs NANOMEDICINE AND NANOBIOTECHNOLOGY WILEY

High spin Fe(III)-doped nanostructures as T_1 MR imaging probes

Mauro Botta[1] | **Carlos F. G. C. Geraldes**[2,3] | **Lorenzo Tei**[1]

[1]Department of Science and Technological Innovation, University of Piemonte Orientale, Alessandria, Italy

[2]Faculty of Science and Technology, Department of Life Sciences and Coimbra Chemistry Center, University of Coimbra, Coimbra, Portugal

[3]CIBIT—Coimbra Institute for Biomedical Imaging and Translational Research, University of Coimbra, Coimbra, Portugal

Correspondence
Carlos F. G. C. Geraldes, Faculty of Science and Technology, Department of Life Sciences and Coimbra Chemistry Center, University of Coimbra, 3000-393 Coimbra, Portugal.
Email: geraldes@ci.uc.pt

Funding information
Coimbra Chemistry Center, Grant/Award Numbers: POCI-01-0145-FEDER-027996, UID/QUI/00313/2019; Ministero dell'Università e della Ricerc, Grant/Award Number: PRIN 2017A2KEPL

Edited by: Gareth Williams, Associate Editor and Nils G. Walter, Co-Editor-in-Chief

Abstract

Magnetic Resonance Imaging (MRI) T_1 contrast agents based on Fe(III) as an alternative to Gd-based compounds have been under intense scrutiny in the last 6–8 years and a number of nanostructures have been designed and proposed for in vivo diagnostic and theranostic applications. Excluding the large family of superparamagnetic iron oxides widely used as T_2-MR imaging agents that will not be covered by this review, a considerable number and type of nanoparticles (NPs) have been employed, ranging from amphiphilic polymer-based NPs, NPs containing polyphenolic binding units such as melanin-like or polycatechols, mixed metals such as Fe/Gd or Fe/Au NPs and perfluorocarbon nanoemulsions. Iron(III) exhibits several favorable magnetic properties, high biocompatibility and improved toxicity profile that place it as the paramagnetic ion of choice for the next generation of nanosized MRI and theranostic contrast agents. An analysis of the examples reported in the last decade will show the opportunities for relaxivity and MR-contrast enhancement optimization that could bring Fe(III)-doped NPs to really compete with Gd(III)-based nanosystems.

This article is categorized under:

Diagnostic Tools > In Vivo Nanodiagnostics and Imaging

Diagnostic Tools > Diagnostic Nanodevices

Therapeutic Approaches and Drug Discovery > Nanomedicine for Oncologic Disease

KEYWORDS

contrast agents, iron(III)-based nanostructures, magnetic resonance imaging, multifunctional nanoparticles

1 | INTRODUCTION

Over the last 20 years, functionalized nanoparticles (NPs) have emerged as an advantageous alternative to traditional diagnostic and therapeutic approaches for several reasons: (i) NPs are able to incorporate or conjugate to a large number of imaging or therapeutic agents thanks to their sizeable compartments (large interior loading volume and/or

surface area); (ii) they have the possibility to integrate more than one kind of imaging or therapeutic agents allowing to act as multimodal nanoplatforms for diagnostic or theranostic purposes; (iii) they can be functionalized on the surface with PEG or hydrophilic polymers to increase stealth properties, hence the circulation time, or with targeting moieties to direct the nanoprobes to specific disease sites for drug delivery and imaging. These features provide multifunctional NPs with great potential as innovative diagnostic and therapeutic probes for the clinical field and preclinical research. The number and type of NPs employed for drug delivery and imaging is extensive, ranging from organic-based (e.g., proteins, liposomes, micelles, dendrimers, solid lipid nanoparticles), inorganic-based (e.g., iron oxide NPs, gold NPs, semiconductor nanocrystals, silica NPs) and hybrid nanoparticles. NPs with well-defined size and shape can be designed and synthesized. The overall size of the NPs is a relevant parameter to be considered as it largely determines their fate in vivo: those with a mean diameter below 5 nm are usually eliminated through renal excretion, whereas larger particles (>100 nm) are easily taken up by macrophages and then undergo hepatobiliary excretion (Antwi-Baah et al., 2022; Das, 2021; Doane & Burda, 2012; Gao et al., 2016; Key & Leary, 2014; Smith & Gambhir, 2017).

Among the imaging techniques, Magnetic Resonance Imaging (MRI) is a non-invasive diagnostic modality with excellent contrast ability and high spatial and temporal resolution that provides detailed information about soft tissues and organs. However, its low sensitivity has prompted the development of nanostructured MRI contrast agents (CAs) that allow increasing dramatically the sensitivity of the technique and reducing the injected dose for signal enhancement (Wahsner et al., 2019).

In very general terms, MR images depend on a complex combination of parameters relating to proton density (PD) and longitudinal (T_1) and transversal (T_2) relaxation times. However, as well highlighted by S. Koenig already 30 years ago: "MR images based solely on water proton density will have little contrast. The remarkable success of MRI as a clinical tool derives from the serendipitous fact that the values of both the longitudinal and transverse relaxation rates, $1/T_1$ and $1/T_2$, of water protons of different tissues can differ by as much as a factor of two at anyone value of imaging field, and are relatively tissue-specific." (Koenig, 1988) It follows that MRI images prevalently represents maps of tissue-specific relaxation rates of the protons of tissue water. In a real experiment, the signal that is measured in MRI is determined by the type of pulse sequence used and contains information on both PD and relaxation times T_1 and T_2. To manipulate and/or optimize the contrast of the image in the tissues investigated, the data are weighted by T_1 or T_2 to a different extent according to the needs or preferences. In practice, tissues characterized by long values of T_1 and T_2 (like the protons of mobile water molecules) are dark in a T_1-weighted image while they appear bright in the corresponding image acquired with a T_2-weighted sequence. On the other hand, tissues characterized by short T_1 and long T_2 appear bright in a T_1-weighted image and gray in the T_2-weighted image.

As for the effect of contrast-enhancing agents, the T_1-shortening contrast agents (T_1-CAs) make the signal brighter (positive contrast), while the T_2-shortening contrast agents (T_2-CAs) reduce the intensity of the signal (darker image; negative contrast). T_1-CAs are typically small complexes of paramagnetic ions characterized by long electronic relaxation times, such as Gd(III), Mn(II) or Fe(III) (Geraldes & Laurent, 2009; Wahsner et al., 2019). Typical T_2-CAs are the superparamagnetic nanoparticles like SPIO and USPIO or the paramagnetic complexes of metal ions such as Dy(III) or Tm(III), characterized by high magnetic moment values and very short electronic relaxation times (Vander Elst et al., 2002).

The most investigated nanosystems for T_1-weighted MRI are Gd-based, with several Gd(III) complexes incorporated into (or conjugated to) the nanocarriers or with Gd^{3+} ions being part of the inorganic nanostructure. To achieve the best efficiency, the complex must contain a number of water molecules coordinated to the metal centre equal to or greater than one (hydration number $q \geq 1$), in rapid exchange ($k_{ex} = 1/\tau_M$; τ_M is the mean residence lifetime of the metal-bound water molecule) with the bulk water. The high loading of active paramagnetic centers increases the efficiency of the probe, in particular in the magnetic field range 0.5–2 T, due to the increased molecular volume of the nanoprobe associated with a marked reduction of the global tumbling motion rate, $1/\tau_R$, where τ_R is the overall rotational correlation time of the system (Botta & Tei, 2012). In the last decades, a broad variety of Gd-based nanosystems have been investigated and there are several excellent and comprehensive reviews that examined in detail the preparation, properties, and applications of these nanosized Gd-based CAs (Villaraza et al., 2010). Although clinically applied Gd(III) chelates are considered very safe and very well tolerated by patients, in recent years Gd-based CAs (GBCAs) have been associated with two clinical concerns that have prompted the research to explore safer alternatives. Thus, in 2006, nephrogenic systemic fibrosis (NSF) was correlated with the release of Gd^{3+} ions from insufficiently stable MRI CAs in patients with impaired renal clearance (High et al., 2007); then, more recently, the retention of tiny amounts of Gd in the tissues of patients exposed to multiple MRI scans was highlighted (Gianolio et al., 2017). Although studies on nanosystems for MRI are still in

the preclinical phase, even in the field of nanoprobes there is an initial shift of the research toward the use of other paramagnetic ions, such as Mn(II/III) and Fe(III).

Iron has a stable iron(III) oxidation state, with $3d^5$ high spin configuration and is an essential element involved in many metabolic processes and present in serum at a concentration of 100–200 μg/L. However, it is important to avoid the presence of the free metal ions, as Fe(II) can form free radicals (Fenton reaction) and its concentration in body tissues must be tightly regulated because in excessive amounts, it can lead to tissue damage (LD_{50} of FeEDTA [rat, oral] = 1.3 g/kg; EDTA = Ethylenediamine tetraacetic acid; Whittaker et al., 2002). Iron(III) has been mainly investigated in the form of superparamagnetic iron oxide nanoparticles (SPIONs), which have primarily been applied as negative CAs for T_2 MRI applications (Laurent et al., 2008). Very recently, small molecular weight Fe(III) chelates have received increasing attention to verify if they can represent an effective, viable and safer alternative to the widespread use of GBCAs (Snyder et al., 2020). However, to the best of our knowledge, an updated review on the use of Fe(III) ions as T_1 MRI probes within nanostructures designed and investigated for in vitro studies or preclinical investigations has not yet been published. Several interesting systems have been proposed and studied in the last 6–8 years and the purpose of this review is to present and comment on the variety, complexity and potential of these nanosystems. In this contribution, we will not examine iron oxide or ferrite NPs as these have been extensively and recently reviewed (Alphandéry, 2019; Peters, 2020; Reynders et al., 2021).

2 | IRON(III): GENERAL PROPERTIES

High spin iron(III) complexes are very common with all weak field donor atoms. A large number of Fe(III) complexes are known in which octahedral coordination is prevalent, although notable exceptions exist where the ion is heptacoordinate. In the high-spin complexes, the magnetic moments are typically very close to the spin-only value of 5.9 BM because the ground state (derived from the ^6S state of the free ion) has no orbital angular momentum and there is no effective mechanism for introducing any coupling with excited states. Electron relaxation times have been reported in the range of approximately 10^{-11} s to 10^{-9} s, for example as recently found for the complex $[Fe(EDTA)(H_2O)]^-$(Baranyai et al., 2021). Zero-field splitting (ZFS) is relatively small and its modulation through solvent molecules collisions is likely to represent the main electron relaxation mechanism (Bertini et al., 2016). The ionic radius of Fe^{III} cations is equal to 0.64 Å (in hexacoordinated complexes; CN = 6), much shorter than those of Mn(II) and Gd(III), equal to 0.80 (CN = 6) and 1.00 Å (CN = 9), respectively (Marcus, 1988). This implies a shorter distance between the metallic centre and the protons of the coordinated water, $r_{M\text{-}H}$, which assumes a value of ~2.6–2.7 Å (Mn: ~2.8; Gd: ~3.0 Å). Given the proton relaxivity dependency on the inverse of the sixth power of this distance, we might expect the lower value of the magnetic moment of Fe(III) to be at least partially counterbalanced by the shorter value of $r_{M\text{-}H}$. Data on the value of the coordinated water exchange rates, k_{ex}, are very scarce, but a recent report on complexes with EDTA and CDTA (CDTA = *trans*-1,2-diaminocyclohexane-*N*,*N*,*N*′,*N*′-tetraacetic acid) suggests that the k_{ex} values are high enough not to represent a limit to relaxivity (Baranyai et al., 2021; Table 1).

Therefore, the main distinguishing feature of Fe(III) complexes, compared with the related Gd(III) and Mn(II) chelates, is the occurrence of shorter electronic relaxation times (T_{1e}). This implies that the proton relaxivity is rather low in the proton Larmor frequency range 0.01 to ca. 30 MHz (where the global correlation time receives a sizeable contribution from T_{1e}) and then increases at higher fields as T_{1e} increases. Given the current tendency to install MRI scanners with increasing magnetic field strength, Fe(III) complexes can therefore represent a good opportunity for the development of CAs alternative to GBCAs and characterized by rather comparable relaxivity values.

Iron ions are a necessary and among the most abundant trace elements, used by (almost) all living organisms. In particular, iron is an essential trace element for the human body. As a biometal, it is essential for life, especially for its electron donor and acceptor capabilities that allow the redox process from ferrous ions (Fe^{2+}) to ferric ions (Fe^{3+}). Even free iron ions, like most metal ions, are highly toxic to the human body and therefore their absence from the bloodstream is ensured by a complex transport and storage system (Shander et al., 2009). Therefore, the total body iron (TBI) is strictly regulated. A normal adult male has an iron load of 35–45 mg/kg of body weight, which corresponds to a TBI value of approximately 3–4 g for a weight of 80 kg (Andrews, 1999). Approximately 65% of the total iron in the body is located in hemoglobin in red blood cells (30 mg/g), 4% is coordinated to myoglobin molecules (4 mg/g), 30% is stored as ferritin or hemosiderin in the spleen, bone marrow and liver (men: 10–12 mg/kg; women: 5 mg/kg), while part of the iron circulates in the serum (3 mg) occupying transferrin sites. Through a normal diet we take in about 15 mg of iron

TABLE 1 Main chemical and physical properties of paramagnetic ions used in T_1-weighted MRI

Metal ion	Configuration	Spin-only magnetic moment (μB)	Ionic radius (Å)	Coordination number	Electronic relaxation times (s)	$M - H_w$ distance (Å)
Fe(III)	d^5	5.9	0.64	6–7	10^{-11} to 10^{-9}	2.6–2.7
Mn(II)	d^5	5.9	0.80	6–7	10^{-10} to 10^{-8}	~2.8
Gd(III)	f^7	7.9	1.00	8–9	10^{-10} to 10^{-8}	~3.0

per day of which only ca. 10% is actually absorbed. In addition, iron is less toxic than most of the metals (Williams et al., 1982).

In conclusion, iron-based contrast agents appear to possess considerable potential for both favorable magnetic properties and improved toxicity profile. Several small molecule Fe(III) complexes possess high biocompatibility and stability under physiological conditions and a number of iron chelates are already used for the treatment of iron overload disease (Kalinowski & Richardson, 2005) and cancer (Yu et al., 2012).

3 | MRI T_1 CONTRAST AGENTS BASED ON IRON(III) NANOSYSTEMS

Although the consideration of Fe(III) as a realistic alternative to Gd-based compounds is very recent, a number of nanosystems have been designed, characterized and reported in the last 6–8 years. Microorganisms use low molecular weight chelating agents (siderophores) capable of tightly coordinating iron, solubilizing it and making it available for transport (Raymond et al., 2015). The chelating agents can be hydroxamates, substituted catechols, or derived ligands that combine these coordinating units. These ligands are characterized by a high degree of specificity and form very stable complexes with Fe(III) ions. It is therefore not surprising that in many of the cases reported in the literature and described in this review, the Fe(III) ions used as T_1 MRI paramagnetic probes have been incorporated into structures containing these types of structural units. The most common are shown in Scheme 1.

In this review, a few recent examples of Iron(III)-based nanosystems are discussed, classified according to their chemical composition, and whose main characteristics are summarized in Table 2.

3.1 | Amphiphilic polymer-based NPs

An early and innovative investigation concerns the use of Fe(III) as a T_1 relaxation agent for MRI (Starmans et al., 2015). In this study, H. Grüll et al. examined the potential of ^{89}Zr-deferoxamine (DFO) and Fe^{3+}-labeled micelles nanoplatform (^{89}Zr/Fe-DFO-micelles) for dual modality positron emission tomography (PET)/MR imaging. The use of various block copolymers allows a modular approach to the design of NPs such as micelles, for example by incorporating hydrophobic drugs in the inner core and linking imaging probes and targeting moieties (e.g., antibodies and peptides) to the outer shell (Lee et al., 2010). The novel ^{89}Zr/Fe-DFO micelles allow for T_1-weighted MRI experiments, unlike the vast majority of previously developed PET/MRI and single-photon emission computed tomography (SPECT)/MRI systems that were based on radiolabelled iron oxides, therefore suitable as T_2-specific MRI contrast agents. The micelles were prepared through the self-assembling of a mixture of polybutadiene-b-polyethylene oxide (PBD-b-PEO) and polybutadiene-b-polyacrylic acid (PBD-b-PAA) polymers, while the use of acrylic acid (AA) residues allowed to functionalise the nanoparticles with ^{89}Zr-DFO (for PET imaging) and Fe^{3+}-DFO (for MRI). Even if the micellar nanoparticles are eliminated through the liver and spleen, the use of Fe(III) as paramagnetic metal ion instead of commonly used Gd(III) avoids any toxicity problems possibly associated with the potential release of Gd(III) from the nanosystem (Langereis et al., 2013). The relaxivity studies for the Fe-DFO-micelles (37 °C, 1.41 T) indicated modest values of longitudinal (r_1) and transversal (r_2) ionic relaxivities of 2.7 and 3.1 mM^{-1} s^{-1}, respectively. However, the authors estimated values of r_1 and r_2 per mM micelle of 1620 and 1860 mM^{-1} s^{-1}, respectively. The most relevant indication of this study is that Fe-DFO micelles have an efficacy as T_1 agents not too different from that of analogous systems based on Gd(III) (Figure 1). On the other hand, these Fe-based systems do not present potential toxicity problems and are therefore more suitable for clinical translation. It is worth noting that the net iron load administered in this

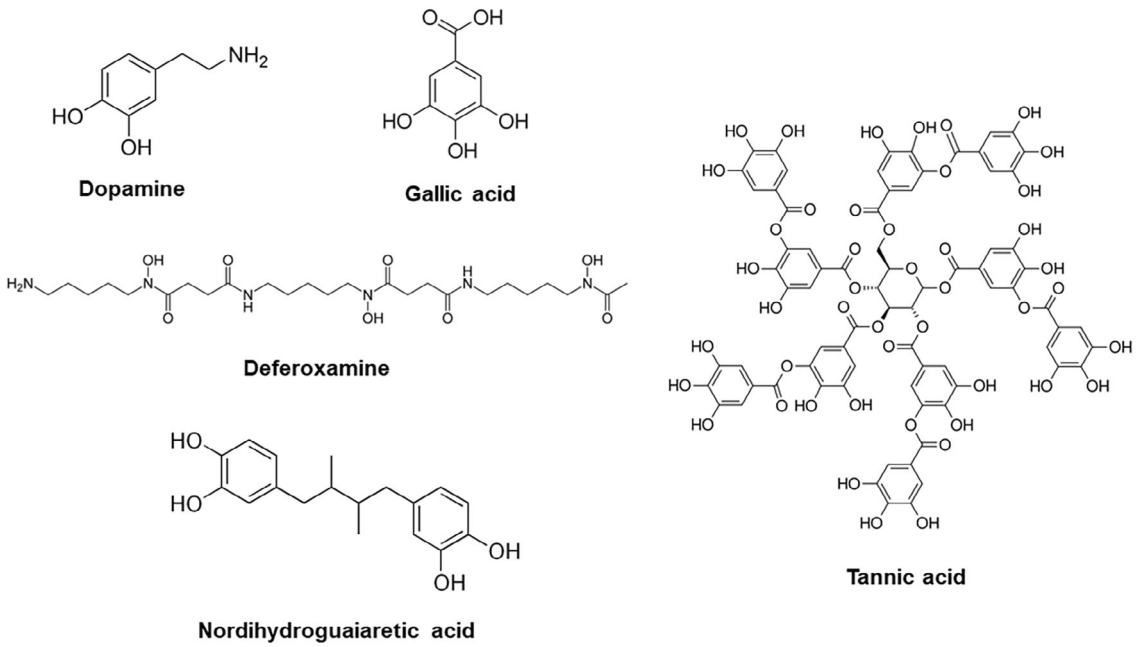

SCHEME 1 Chelating chemical structures used for the preparation of Fe(III)-based nanosystems.

study is only a small fraction (∼5%) of the total amount of iron present in the body and comparable to that associated with the clinical use of iron oxides in T_2 MRI.

In a more recent study, a different formulation was examined which consists of paramagnetic iron(III)-chelated poly(lactic-co-glycolic) acid (PLGA) nanoparticles (Marasini et al., 2021). One of the reasons for this design is related to the fact that the polymer and phospholipids used for the preparation of NPs represent biodegradable and biocompatible components. Fe–PLGA nanoparticles were analyzed with TEM and showed to be highly monodisperse, with a uniform spherical-shape and an average diameter of ca. 93 nm. Moreover, the NPs resulted to have an average hydrodynamic size of ca. 130 nm and to be characterized by long-term stability in PBS and serum. Strong chelation of Fe^{3+} ions was inferred from experiments that showed a release of only 3.1% of iron over 72 h of incubation in simulated body fluid. Longitudinal relaxivities of the NPs in aqueous solution at neutral pH were $r_1 = 10.6$ and 3.0 $mmol^{-1}\ s^{-1}$ at 3.0 and 14.1 T, respectively. The in vivo contrast efficacy of Fe–PLGA NPs was tested in a murine model by intravenous injection via the lateral tail vein. Dynamic MR images were acquired pre-contrast and after injection at several time points up to 3 h, on a 3 T scanner. An angiographic map was obtained that demonstrates the good contrast enhancement in T_1-weighted experiments.

Very recently, Shunmugam reported an original application involving the development of dual-imaging polymer-based mitochondrial theranostic systems containing an integrated fluorescence-MR imaging agent (Patra et al., 2022). The polymer was prepared by ring-opening polymerization using three different monomers bearing the chemotherapeutic drug Chlorambucil, the receptor targeting agent biotin, a triphenylphosphonium segment (mitochondriotropic agent), and an iron(III) rhodamine complex (for fluorescence and MR imaging). Due to its amphiphilic character, the polymer spontaneously self-assembles into nanospheres of ca. 200 nm diameter that easily internalize into cancer cells through receptor-mediated endocytosis and rapidly accumulate into mitochondria due to the strong electrostatic interactions. The labelling of the polymer with Fe(III) ions was carried out by adding ferric chloride to the polymer containing rhodamine B suitably modified to allow the coordination of the metal ions. Due to the presence of paramagnetic ions incorporated (complexed) in the polymeric units, the NPs show a good efficacy in increasing the relaxation rate of the solvent protons, with relaxivity values at 500 MHz and 298 K of $r_1 = 14.91\ mM^{-1}\ s^{-1}$ and $r_2 = 65.95\ mM^{-1}\ s^{-1}$. The efficacy of the polymer was assessed by performing fluorescence microscopy and cytotoxicity experiments with MTT and crystal violet staining assays using human cervical, HeLa, and breast, MCF-7, carcinoma cell lines. The data highlighted an enhancement of chemotherapeutic efficacy associated with an effective delivery of the chemotherapeutic drug Chlorambucil into mitochondria.

TABLE 2 Summary of the basic properties of the examples of Fe(III)-based nanosystems as MRI probes and theranostics discussed in this work

Nanoparticles composition	Imaging modalities	Relaxivity (mM^{-1} Fe s^{-1}), Temp, B_o	Therapeutic modalities	Cell/animal model	Hydrodynamic diameter (nm)	References
^{89}Zr/Fe(III)-DFO-PBD-b-PEO/PBD-b-PAA micelles	T_{1w} MRI/PET	$r_1 = 2.7, 3.1$, $r_2 = 3.1$ 310 K, 1.41 T	–	In vivo tumor mice	25	Starmans et al., 2015
Fe(III)-PLGA NPs	T_{1w} MRI	$r_1 = 10.6$ (3.0 T) $r_1 = 3.0$ (14.1 T) 293 K	–	In vivo NU/NU mice	130	Marasini et al., 2021
Fe(III)-rhodamine/Chlorambucil@RD CH PG BN TP polymer	T_{1w} MRI/fluorescence imaging	$r_1 = 14.91$; $r_2 = 65.95$ 298 K, 11.7 T	Chemotherapy	in vitro HeLa and MCF-7 cells	220	Patra et al., 2022
Fe(III)-$(OEG)_m$-$(Cat)_n$-$(C6)_p$ triblock copolymer CMNs	T_{1w} MRI	$r_1 = 7.9$; $r_2 = 11.1$ 310 K, 1.41 T	–	In vitro HeLa cells	25	Li, Huang, et al., 2016a
Fe(III)-synthetic melanin NPs	T_{1w} MRI	$r_1 = 8$ 310 K, 1.88 T	–	In vitro serum and cell culture media	140–250	Li, Xie, et al., 2016b
Fe(III)@PDOPA10-b-PSar50	T_{1w} MRI/MRI angiography	$r_1 = 5.6$ 293 K, 3.0 T	–	In vitro NIH 3 T3 cells In vivo nude mice and rabbits	28.6	Miao et al., 2018
Fe(III)-GA-PVP CPNDs	T_{1w} MRI	$r_1 = 1.5$; $r_2 = 2.9$ 298 K, 1.5 T	PTT	In vitro SW620 cells In vivo SW620 tumor mice	5.3	Liu et al., 2015
GA-Fe@BSA	T_{1w} MRI	$r_1 = 0.89$; $r_2 = 0.95$ 298 K, 0.5 T	PTT	In vivo 4 T1 tumor mice	8.8	Mu et al., 2017
GA-Fe@BSA-PTX	T_{1w} MRI	$r_1 = 1.20$; $r_2 = 1.95$ 298 K, 0.5 T	Chemotherapy/PTT	In vivo 4T1tumor mice	115	An et al., 2018
Fe(III)–TA NPs	T_{1w} MRI	$r_1 = 3.14$ 298 K, T[a]	–	In vivo male Wistar rats	~9.5	Phatruengdt et al., 2020, 2022
Fe(III)-NGDA-dendritic-PEG oligomer NPs	T_{1w} MRI	$r_1 = 3.95$ 298 K, 7 T	–	In vivo brain tumor U251 MG mice	66	Xue et al., 2020
GdF_3:Fe(III)@ PEG NPs	T_{1w}/T_{2w} MRI/X-ray CT	$r_1 = 3.3$; $r_2 = 36.0$ 298 K, T[a]	–	In vivo tumor mice	150–250	Dong et al., 2017
[Gd(III), Fe(III) (7:3)]-TA NPs	T_{1w} MRI	$r_1 = 9.3$; $r_2 = 11.7$ 298 K, 0.94 T	PTT	In vivo EMT-6 tumor mice	~23	Qin et al., 2020
Au@SiO_2-MDOTA-Cy7@Au-mPEG M = Fe(III), Gd(III)	T_{1w} MRI/Fluorescence imaging	$r_1 = 5.9$, $r_2 = 25.1$ (Fe) at 1.5 T; $r_1 = 22$, $r_2 = 54.7$ (Gd) at 4.7 T; 298 K	PTT	In vitro RAW 264.7 macrophages In vivo mice	>100	Henderson et al., 2018

TABLE 2 (Continued)

Nanoparticles composition	Imaging modalities	Relaxivity (mM^{-1} Fe s^{-1}), Temp, B_o	Therapeutic modalities	Cell/animal model	Hydrodynamic diameter (nm)	References
Fe(III)-TOB@ β-glucan particles	T_{1w} MRI	$r_1 = 0.21$; $r_2 = 3.45$ 310 K, 4.7 T	–	In vitro water GPs	>1000	Patel et al., 2020
Fe(III)-carbon dots (Fe-CDs)	T_{2w} MRI	$r_1 = 0.13$; $r_2 = 9.9$ 298 K, 9.4 T	–	in vitro U87MG cells In vivo U87MG tumor mice	10.3	Qin et al., 2021
Fe(III)- tris(β-diketonate)@ PFOB NEs	^{19}F T_{1w} MRI	$r_1 = 1.01$; $r_2 = 1.56$ 298 K, 9.4 T	–	in vitro water NEs	140–180	Wang et al., 2019

[a]Not reported.

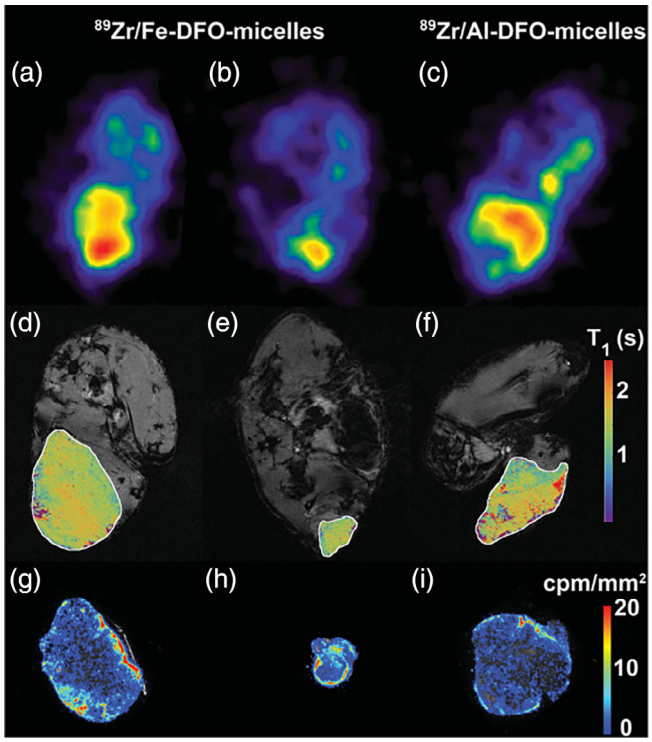

FIGURE 1 Visualization of the intratumoural accumulation of ^{89}Zr/Fe- and ^{89}Zr/Al-DFO-micelles in tumor bearing mice using PET/MRI and autoradiography. Typical in vivo PET images of cross-sections throughout the limbs with predominant A, B) ^{89}Zr/Fe-DFO-micelles and C) ^{89}Zr/Al-DFO micelles tumor uptake. The middle row shows T_1-weighted anatomical MR images (3 T) with quantitative T_1-map overlay D–F) providing insight in the intratumoural distribution of the ^{89}Zr/Fe-DFO-micelles, displaying inhomogeneous intratumoural probe distribution, with lower uptake in the core versus the periphery. The bottom row shows representative ex vivo autoradiography images, displaying lower uptake of G, H) ^{89}Zr/Fe-DFO micelles and I) ^{89}Zr/Al-DFO-micelles in the core of the tumor with respect to the tumor periphery. Reprinted with permission from Adv. Healthcare Mater. 2015, 4, 2137. Copyright 2015 Wiley.

3.2 | NPs containing polyphenolic binding units

It is quite interesting the approach of N. Gianneschi et al. who developed amphiphilic triblock copolymers containing Fe(III)-catecholate complexes (Li, Huang, et al., 2016a). These systems give rise to spherical or cylindrical micellar nanoparticles (SMN and CMN, respectively) which act as T_1-weighted MRI agents with high relaxivity values, low cytotoxicity and long-term stability in biological fluids. In this case, the strong coordination bonds between Fe(III) ions and catechol ligands are exploited to develop self-assembled nanoparticles from amphiphilic block copolymers containing these paramagnetic structural units. The authors aimed to prepare a new class of Gd-free macromolecular contrast agent for T_1-weighted MRI characterized by strictly controlled size, shape and composition. The synthetic procedure is based on post-polymerization functionalization in order to incorporate the catechol groups in the central block of a triblock copolymer amphiphile. By controlling and adjusting the segment size of each block in the amphiphilic copolymers it was possible to obtain stable spherical (SMN) and cylindrical (CMN) micellar systems. The reported $1/T_1$ nuclear magnetic relaxation dispersion (NMRD) profiles as a function of temperature and frequency showed that the r_1 values of these nanosystems are greater than those of the clinically used Gd(III) contrast agents across a wide range of applied magnetic field strengths (>10 MHz) (Botta & Tei, 2012). This enhanced ionic relaxivity (r_1 = 7.1 and 7.9 mM^{-1} s^{-1} at 60 MHz and 310 K for SMN and CMN, respectively) probably arises from the presence of second-sphere water molecules interacting with the Fe(III)-(catecholate)$_3$ units. In addition, the r_2/r_1 ratios of both SMN and CMN (r_2/r_1 = 1.25 for SMN, and r_2/r_1 = 1.40 for CMN) is low and therefore positive contrast enhancement prevails. Both SMN and CMN showed a good stability in biological media, high biocompatibility and low toxicity with respect to live cells. Notably, the authors observed an interesting shape-dependent cellular uptake with CMN featuring brighter contrast and higher relaxation rates than the spherical micelles (Li, Huang, et al., 2016a; Figure 2).

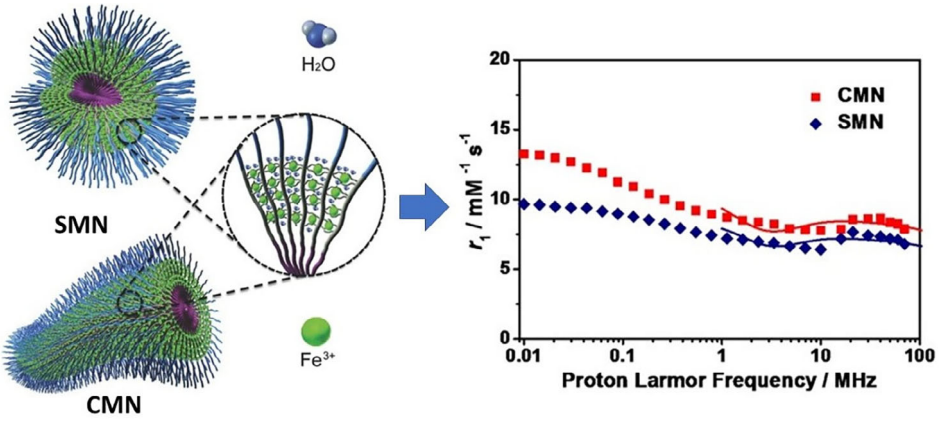

FIGURE 2 Amphiphilic tri-block copolymers containing Fe^{III}-catecholate complexes formulated as spherical- or cylindrical-shaped micellar nanoparticles as new T_1-weighted imaging agents. Relaxivities of both micellar nanoparticles exceed those of established gadolinium chelates across a wide range of applied magnetic field strengths as shown in the NMRD profiles on the right of the figure. Reprinted with permission from Small, 2016, 12, 668. Copyright 2016 Wiley.

Fe(III)-loaded synthetic melanins have also been investigated as potential MRI nanoprobes. The interest in these systems as MRI probes derives from their well-known characteristics of excellent biocompatibility and ability to tightly coordinate paramagnetic metal ions through the catechol-based functional groups. Li et al. developed a synthetic method for improving and controlling the iron loading of synthetic melanin nanoparticles (SMNP) and then carried out an in-depth analysis on their structure–property relationship (Li, Xie, et al., 2016b). To this end, the researchers devised a pre-polymerization doping procedure, using a mixture of Fe(III)(dopamine)$_3$ and free dopamine as precursors for the formation of Fe(III)-chelated SMNPs. Since Fe(III) ions can be continuously incorporated into the SMNP during the polymerization process, variable and high doping levels of metal ions within the particle can be achieved. A series of Fe(III)-doped spherical SMNPs with various Fe(III) concentrations were prepared whose diameter is within the range of 140 to 250 nm. An unexpected and counterintuitive result was obtained from the analysis of ^{1}H NMRD profiles (Aime et al., 2019). Contrary to expectations, the relaxivity values (per particle) over all frequencies do not increase proportionally to the iron load. Instead, there is an upper limit of doping (Fe(III)% = 5.86) beyond which relaxivity decreases. In fact, at higher iron loadings over half of the Fe(III) ions is involved in antiferromagnetic metal–metal coupling interactions, leading to a significant drop in the magnetic moment even at room temperature and thus reducing the relaxivity of the samples. Additionally, the magnetically coupled Fe(III) − Fe(III) interactions can alter the nature of the relaxation, shifting of the SMNPs toward T_2-weighted agents at high concentrations. SMNPs with intermediate iron load show high ionic r_1 values (ca. 7–8 mM^{-1} s^{-1} between 20 and 80 MHz) which increases with increasing frequency. Moreover, the nanoparticles show long-term stability in physiological environment, tested by measuring the signal enhancement in T_1-weighted MR images in different media. Although only in vitro studies have been performed so far, these systems offer interesting perspectives as positive MRI contrast agents. The high values of r_1, increasing with the applied field strength, the remarkable stability and the modulable load of Fe(III) ions are promising properties for further development.

The high affinity and binding capacity of catechol ligands to coordinate Fe^{3+} cations were exploited by Y. Miao et al. to develop another type of nanoparticles. Diblock copolymers of polypeptide-b-polypeptoid were synthesized via the sequential ring-opening polymerization of sarcosine-NTA (sarcosine-NTA = *N*-methylglycine-*N*-thiocarboxyanhydride) and DOPA-NTA (DOPA = 3,4-dihydroxy-L-phenylalanine) (Miao et al., 2018) (Figure 3). The incorporation of paramagnetic Fe(III) cations in the polypept(o)ide micelles was carried out by solvent exchange. The micellar nanoparticles of Fe^{3+}@PDOPA-b-PSar behave as effective T_1-weighted MRI contrast agents thanks to the strong chelation of Fe(III) cations by catechol ligands. The properties of NPs can be optimized by searching for the best ratios of hydrophobicity and hydrophilicity, that is, the ratios of PDOPA and PSar segments. The best result is represented by PDOPA10-b-PSar50 which exhibits an ideal block composition to form the most stable Fe^{3+}@PDOPA10-b-PSar50 nanoparticles, labeled as NPDS1. The longitudinal relaxivity, r_1, of NPDS1 was measured to be 5.6 mM^{-1} s^{-1} at 3.0 T and 293 K. The authors investigated the in vivo time-course positive MRI contrast by injecting 300 μl of NPDS1 solution (3.0 mg ml^{-1}) in saline via the lateral tail vein of nude mice. They observed that the blood vessels on T_1-weighted MRI rapidly

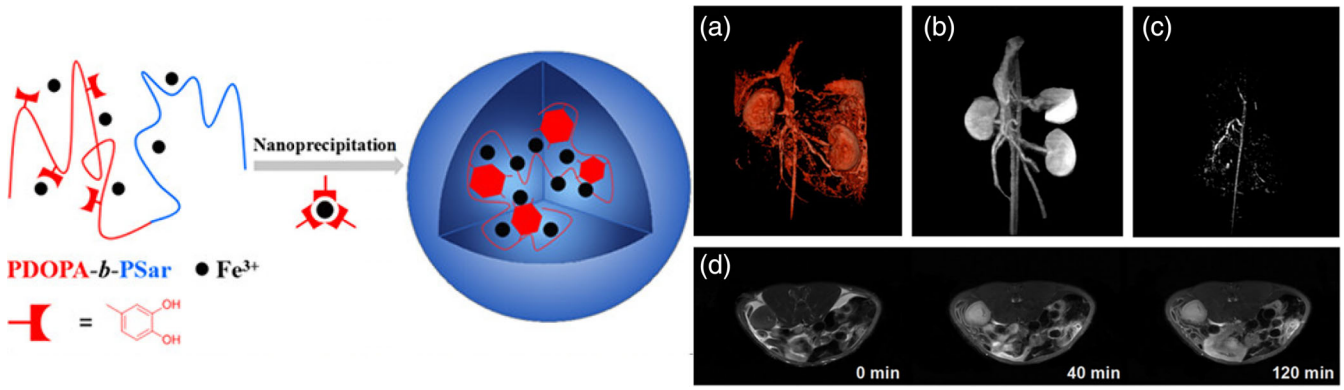

FIGURE 3 Left: Schematic synthesis of the Fe3 + @PDOPA-b-PSar NPs; right: (a) volume rendering MR image of abdominal aorta and inferior vena cava. (b) Maximal intensity projection (MIP) MR image of abdominal aorta and inferior vena cava. (c) MIP image of the separated abdominal aorta and its branch. (d) Axial time-course MRI images of rabbit abdomen. Reprinted with permission from ACS Macro Letters, 2018, 7, 693. Copyright 2018 American Chemical Society.

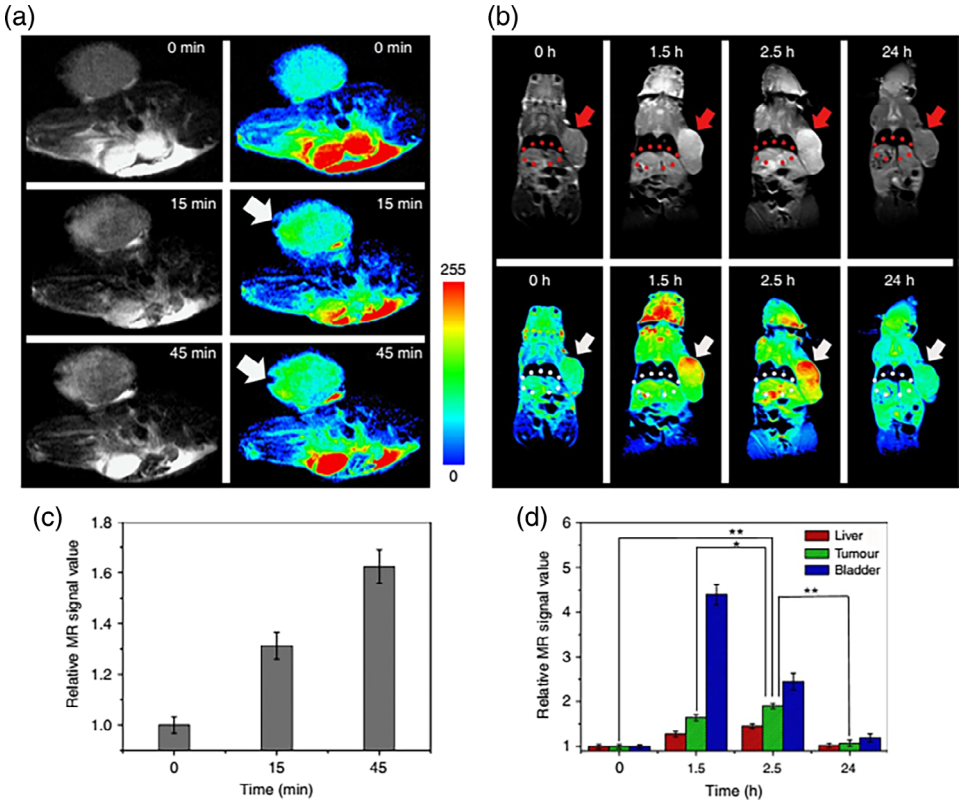

FIGURE 4 In vivo MR images of nude mice bearing colorectal tumors after (a) intratumour injection (injection site, arrows) and (b) intravenous injection (tumor, arrows; liver, ellipses) of Fe-CPNDs at different time intervals (0 min and 0 h indicate pre-injection). (c) Corresponding data analysis of the tumor in "a". (d) Corresponding data analysis of the tumor, bladder, and liver in b. Error bars indicate the SD (n ¼ 5, $^{**}p < 0.01$ or $^{*}p < 0.05$ from an analysis of variance with Tukey's post-test). The tumors are ~700 mm^3 in volume. Reprinted from Nature Communications, 2015, 6, 8803; under creative commons CC BY license.

enhanced within 30 min, and then the enhancement gradually decreased until the wash out of NPDS1, which was completed after 150 min. As expected, with progressive accumulation of nanoparticles into the hepatic region, the liver signal-to-noise ratio increases rapidly until a high value is reached which remains constant. In addition, in vivo MR angiography of rabbits was performed by the injection via ear vein of 10 ml NPDS1 solution (6.0 mg ml^{-1}). After the

injection of NPDS1, axial MR images show good and persistent enhancement at kidneys and vessels for over 120 min (Figure 3).

A high cell viability over 85% indicates very low toxicity with NIH 3T3 cells. Finally, these nontoxic Fe^{3+}-polypept (o)ides nanoparticles were claimed to be clinically promising to replace traditional Gd^{3+} compounds in diagnostic angiography and further tumor imaging (Miao et al., 2018).

F. Liu et al. developed ultrasmall (5.3 nm) and pH-activated nanodots (Fe-CPNDs) composed of coordination polymers synthesized through coordination reactions among Fe^{3+}ions, gallic acid (GA) and poly(vinylpyrrolidone) (PVP) at room temperature (Liu et al., 2015). The Fe-CPNDs are characterized by an electrically neutral surface, which minimizes interactions with serum proteins and other species in blood, and exhibit a pH-activatable MRI contrast as well as a remarkable photothermal activity. In vivo animal experiments showed that the Fe-CPNDs accumulated in the tumor tissue via the enhanced permeability and retention (EPR) effect and were completely excreted via the renal pathway 24 h after tail-vein injection. The combination of a short residence time in the organism associated with renal clearance, which minimizes the risk of toxicity, and preferential accumulation in the tumor area meet some key requirements for potential clinical applications (Figure 4). The coordination between Fe^{3+} and GA changes with pH, with more hydrated species (greater relaxivity) prevailing in more acidic conditions. The low pH of the tumors is therefore able to activate the Fe-CPNDs thus enhancing the MRI contrast. (Mi et al., 2016). In addition, these NPs strongly absorb light in the visible to near-infrared regions and show an excellent photothermal effect (Li et al., 2020). In vivo photothermal therapy (PTT) studies were performed to evaluate the anticancer efficacy of Fe-CPNDs in a xenograft tumor mouse model. Tumor growth was completely inhibited using a Fe-CPND concentration of 0.2 mg/kg. The results of this study indicate that Fe-CPNDs may represent a new class of promising renal-clearable nanoprobes for photothermal therapy and molecular imaging (Liu et al., 2015).

Fe(III)-based nanosystems have also been studied and proposed as protein-related nanotheranostic agents. For the development of nanotheranostic agents, the organic platforms offer clear advantages over inorganic platforms as they contain benign components and are easily degraded, thus offering higher biological compatibility. In particular, the development of biodegradable and protein-related nanotheranostic agents appears very promising for the goal of clinical applications. Bovine serum albumin (BSA) was used as a coating of nondegradable inorganic nanoparticles or as a surfactant to control the synthesis of transition metal ion-based NPs, a process reminiscent of the typical biomineralization. Along this line, Mu et al. investigated the BSA-assisted synthesis of gallic acid-Fe(III) coordination polymer NPs for cancer theranostics (Mu et al., 2017). The BSA-coated GA-Fe (GA-Fe@BSA) NPs are ultrasmall (3.5 nm) and characterized by good biocompatibility, have a low r_2/r_1 ratio (1.06) which identifies them as MRI probes for T_1-weighted images, and maintain strong absorption in the visible to near-infrared regions. The ultrasmall dimensions were attributed to the occurrence of a strong coordination between Fe^{3+} and BSA. In the in vivo study, pronounced signal changes in T_1-weighted MRI were observed in tumor-bearing mice before and after intratumour injection with GA-Fe@BSA. These NPs were also shown to be capable of efficiently destroy solid tumors following treatment with laser ablation.

The same research groups further developed these systems with the aim of increasing tumor accumulation while maintaining pronounced characteristics of biodegradability and biocompatibility. To this end, they employed the drug paclitaxel (PTX) to assemble BSA-coated ultrasmall GA-Fe@BSA NPs exploiting the hydrophobic effect to obtain large GA-Fe@BSA-PTX self-assembled multifunctional theranostic NPs (An et al., 2018). This nanosized platform offers a number of advantages: (a) an improved MRI contrast capability associated with the larger size (∼115 nm; greater number of paramagnetic centres); (b) more effective tumor uptake; (c) the chemotherapeutical property of PTX enable the inhibition of tumor growth at a lower dosage; (d) the possibility of using a dual therapeutic method such as PTT and chemotherapy. In vivo studies confirmed enhanced MRI performance and tumor accumulation (Figure 5). Furthermore, the GA-Fe@BSA-PTX self-assembled NPs showed an easy clearance from the body: they first accumulated in the liver and subsequently, through the bloodstream, reached the kidney, bladder and finally urine.

NPs of iron–tannic acid complexes (FT NPs) were prepared and examined to evaluate their potential for detecting liver pre-neoplasia (Phatruengdet et al., 2020). These nanoparticles are characterized by several favorable properties such as small size, high MRI contrast ability, high stability, good water solubility, and high uptake efficiency in tumor cells. The in vivo study revealed that FT NPs are able to enhance MRI signals in rat livers with pre-neoplastic lesions within 60 min postinjection. Furthermore, initial tests indicated low toxicity. In a more recent study, these NPs were used for a quantitative MRI-derived liver function assessment and for enhancing clearance function in liver parenchyma (Phatruengdet et al., 2022). In short, in T_1-weighted experiments the maximum MRI signal enhancement was detected 30 min post-injection and thereafter decreased. The decrease in signal intensity reflects the FTs metabolism by

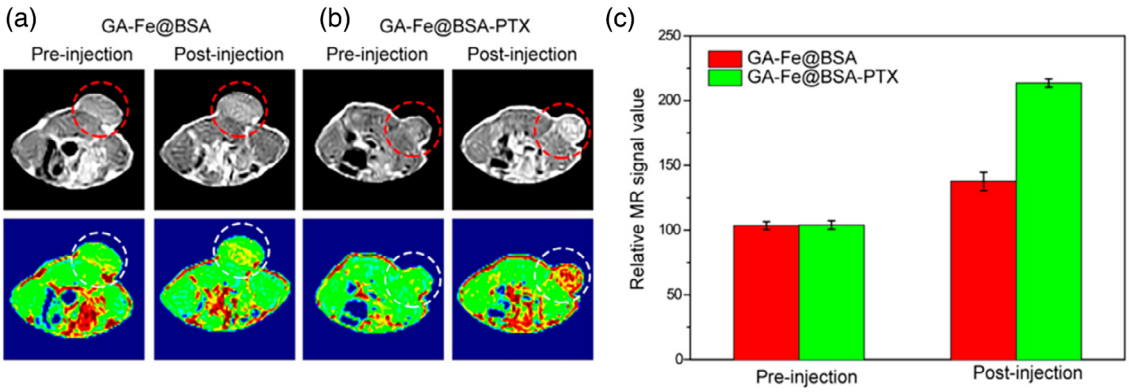

FIGURE 5 MRI of the tumor pre- and post-intratumoural injection of (a) ultrasmall GA-Fe@BSA nanoparticles and (b) GA-Fe@BSA-PTX self-assembled nanoparticles and (c) corresponding relative signal values. Reprinted with permission from ACS Applied Materials and Interfaces, 2018, 10, 28483. Copyright 2018 American Chemical Society.

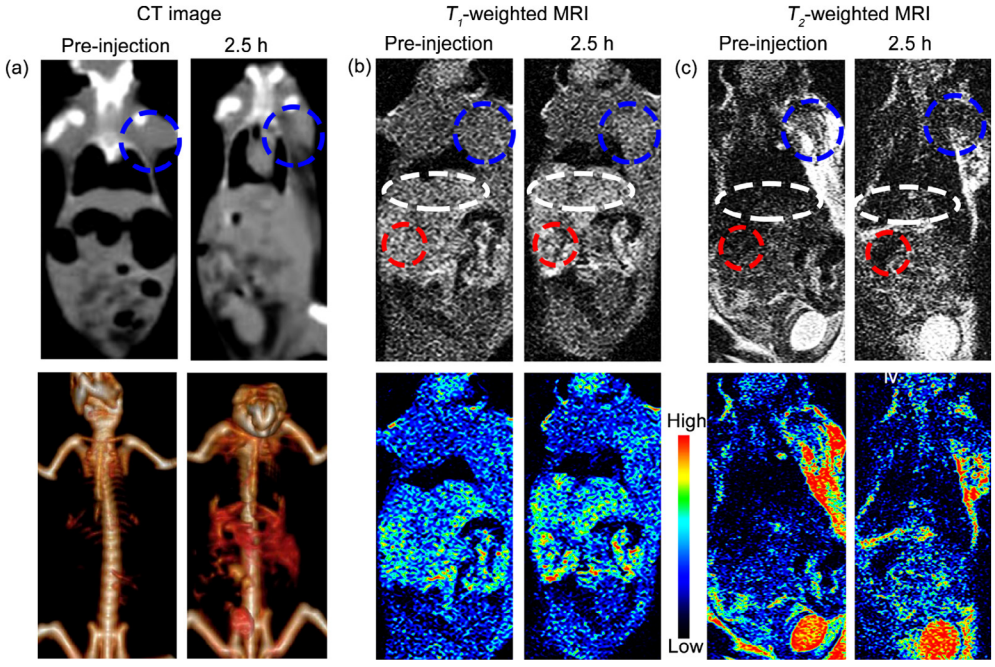

FIGURE 6 In vivo CT images (a), T_1-weighted MRI (b), and T_2-weighted MRI (c) of tumor-bearing mice after intravenous injection of PEG-GdF_3:Fe NPs at timed intervals (tumor, blue circles; liver, ellipses; spleen, red circles). Reprinted with permission from ACS Applied Materials and Interfaces, 2017, 9, 20426. Copyright 2017 American Chemical Society.

the liver, a process whose rate constant can be determined. Thus, this parameter can be used to monitor liver clearance function.

In the search for safer alternatives to the use of GBCAs, other iron-based nanoparticles were designed in order to achieve high accumulation in the tumor (high ratio between tumor tissue and normal tissue: TNR), to preserve a sufficiently long retention time within tumors and to possess longer effective imaging windows for the diagnosis. Li and co-workers developed a novel iron-based nanosized contrast agent (IBCA) based on novel telodendritic molecules composed of a hydrophilic polyethylene glycole (PEG) tail and a hydrophobic iron-based dendritic oligomer (Xue et al., 2020). The PEG tail is attached to the dendritic oligomer by iron coordination with the catechol functional groups on nordihydroguaiaretic acid (NDGA) to form a telodendritic structure. This amphiphilic structure is able to self-assemble into a micellar nanostructure in which the coordinated Fe(III) ions are responsible for the good T_1 relaxing ability (r_1 ca. 4 mM^{-1} s^{-1} at 7 T). This MRI nanoprobe showed pronounced selective accumulation at tumor sites and

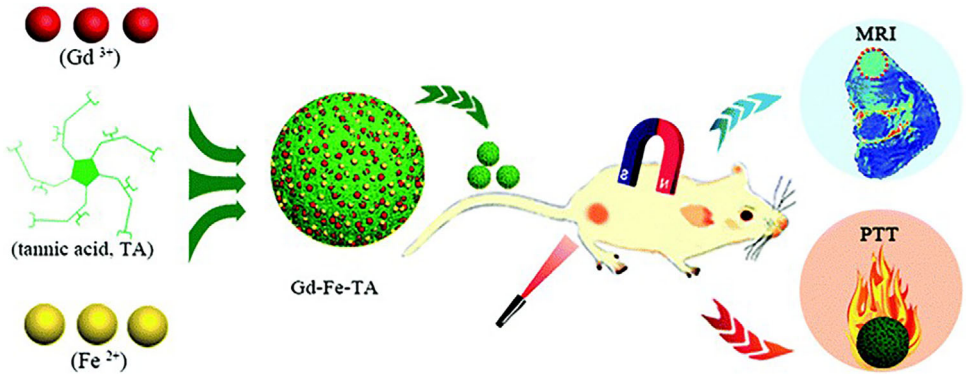

FIGURE 7 Schematic illustration of the synthesis and theranostic applications of bimetallic–phenolate coordination polymer nanoparticles. Reprinted with permission from Nanoscale, 2020, 12, 6096. Copyright 2020 Royal Chemical Society.

markedly improved TNR values. The effective imaging window of this IBCA appears to be of the order of 24 h, much higher than that of small metal complexes, as well as demonstrating an excellent safety profile, high selectivity, and low levels of kidney accumulation.

3.3 | Mixed metals NPs

Interesting nanosystems containing variable amounts of Gd(III) and Fe(III) were proposed in order to develop contrast agents for multifunctional imaging and/or integrate the diagnostic and therapeutic functions (Dong et al., 2017). Both ions are paramagnetic and provide good T_1 and T_2 relaxation effects, while the relatively high X-ray absorption coefficient of Gd(III) also allows for bright images in CT imaging (Ahmad et al., 2015) (Figure 6). Then, the incorporation of Fe^{3+} ions into the crystal lattice of the GdF_3 matrix and the coating with PEG chains allowed to obtain NPs (PEG-GdF_3:Fe) endowed with interesting characteristics as imaging probes: (1) MRI and X-ray computed tomography (CT) multimodal imaging capability; (2) good contrasting efficiency in T_1- and T_2-weighted MRI images; (3) good biocompatibility; and (4) easy and reproducible synthetic procedure. In an in vivo study, the authors followed the time-dependent biodistribution by T_1 and T_2 dual-mode MRI after intravenous injection of tumor-bearing mice. The PEG-GdF_3:Fe NPs appear to accumulate in tumor thanks to the EPR effect. A T_1 signal enhancement was detected in tumor tissues 1.5 h postinjection, which completely vanished after a period of 2.5 h after injection (Figure 6). In addition, these nanoparticles demonstrated a remarkable ability to enhance the contrast in in vivo X-ray CT imaging experiments, at doses lower than those of clinical agents.

In another study, Wei et al. proposed the use of bimetallic (Gd, Fe)–phenolate coordination polymer (CN) nanoparticles (Qin et al., 2020). This approach allows to effectively integrate the advantages of Fe- and Gd-based coordination polymers and combine a good diagnostic technique (T_1-weighted MRI; Gd) with a high therapeutic efficiency associated with photothermal therapy (PTT; Fe-phenolate). To this end, nanoparticles based on bimetallic coordination polymers Gd/Fe–phenolate were prepared through a controllable process that uses $GdNO_3$ and $FeSO_4$ as a source of metal and plant polyphenols (such as tannic acid, TA) as a ligand (Figure 7). Through a process of optimization of the molar Gd/Fe ratio (7:3), the authors were successful in obtaining bimetallic–phenolate CNs characterized by an ultrasmall hydrodynamic diameter (~23 nm), high colloidal stability, a good r_1 value (9.3 mM^{-1} s^{-1}; 40 MHz) with a low ratio r_2/r_1 (1.26) and high photothermal conversion efficiency ($\eta = 37\%$). An in vivo study was also performed: Gd–Fe (7:3)–TA solution (4 mg/kg) was injected via the tail vein to EMT-6 tumor bearing mice and the highest signal enhancement was observed after 4.0 h post-injection. At the same time, this formulation showed significant PTT efficiency in inhibiting tumor growth.

Additional experiments were carried out to evaluate the biodistribution and elimination of these NPs. By collecting the urine and feces of mice at different time intervals after intravenous injection of Gd–Fe (7:3)-TA and performing inductively coupled plasma mass spectrometry (ICP-MS) and MRI measurements, the authors concluded that most of Gd–Fe (7:3)–TA is excreted via the hepatobiliary pathway (ca. 64% after 60 h), while a minor portion is eliminated via renal filtration (~19%). Finally, The Gd content (ICP-MS) in major organs showed a gradual decrease and nearly disappeared at 72 h post-injection (Qin et al., 2020).

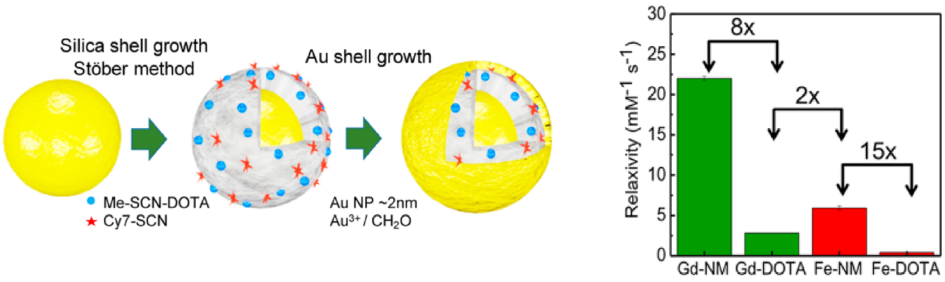

FIGURE 8 Left: Multifunctional fluorescent and MRI-active nanostructure composed of a 50 nm Au core coated with Me-chelates (Me: Gd^{3+}, Fe^{3+}, or Mn^{2+}) and dye molecules embedded in a SiO2 inner shell and a continuous Au outer shell. Right: Graph of the r_1 relaxivity enhancement for Gd-NM (22 ± 0.26 mM^{-1} s^{-1}) and Gd-DOTA (2.8 mM^{-1} s^{-1}) at 4.7 T (green) as compared with Fe-NM (5.9 ± 0.28 mM^{-1} s^{-1} at 4.7 T) and Fe-DOTA (0.4 mM^{-1} s^{-1} at 1.5 T) (red). Reprinted with permission from ACS Nano, 2018, 12, 8214. Copyright 2020 American Chemical Society.

Fe(III) complexes as MRI probes were also incorporated into nanostructures consisting of near-infrared resonant gold nanoparticles to combine imaging and therapy (Henderson et al., 2018). The authors used a multilayer core−shell nanostructure known as a nanomatryoshka (NM), which consists of an Au core, silica spacing layer, and an outer Au shell, for the incorporation of both T_1-weighted MRI contrast agents and fluorescent dye molecules inside the same nanosystem. This structure is characterized by an intense optical absorption close to 800 nm, which is associated with a high photothermal efficiency due to the non-radiative plasmon decay. Paramagnetic metal ions (Gd^{3+}, Fe^{3+} and Mn^{2+}) and appropriate fluorescent dyes were incorporated into the silica layer in order to find the best conditions to optimize both optical and MR imaging properties. To incorporate the paramagnetic centers, the silica layer was doped with SCN-DOTA (DOTA = 1,4,7,10-Tetraazacyclododecane-1,4,7,10-tetraacetic acid), a ligand that provides $q = 1$ Gd(III) and $q = 0$ Fe(III) complexes. At 4.7 T the relaxivity of GdNM NPs (22 mM^{-1} s^{-1}) is increased by eight times compared with that of GdDOTA. Instead, FeNM NPs (5.9 mM^{-1} s^{-1}) show the greatest increase in relaxivity, about 15 times higher than that of FeDOTA (Figure 8). Confocal microscopy imaging data revealed cellular uptake and highlighted non-toxicity in RAW 264.7 macrophage cells. Finally, a preliminary in vivo study showed the presence of both a strong T_1-MRI signal and fluorescence in a mouse model, demonstrating the potential of this nanostructure for dual-modality imaging and the efficacy of an iron-based system that represents a potentially less toxic alternative to the use of Gd-based nanostructures.

3.4 | Miscellaneous NPs

Yeast-derived β-glucan particles (GPs) are widely used for the transport and delivery of a variety of drugs. Of particular interest is the targeting of macrophages, which would allow the administration of drugs to the sites of inflammation, characteristic of various pathological states including cancer or atherosclerosis. Morrow and co-workers encapsulated macrocyclic Fe(III) complexes within the GPs with the aim of providing these particles with MR imaging functionality (Patel et al., 2020). Pentadentate macrocyclic complexes of Fe(III) based on the 1,4,7-triazacyclononane (TACN) ring were efficiently incorporated into GPs, even in the absence of amphiphilic chains. This is explained by the presence of strong electrostatic interactions between the cationic complexes and the negatively charged groups of GPs and, probably, also through the coordination of the metal ion. However, the relaxivity of the Fe-labeled NPs is lower than that of the free complex and this finds a possible explanation in the perturbation of the well-defined network of second-sphere water molecules. A relaxation enhancement is instead associated with the release of Fe-complexes from the particles, and this is possible either by using mildly acidic conditions or by adding a bidentate chelator such as maltol. These preliminary investigations will be followed by a more in-depth study to fine-tune the conditions necessary to ensure the uptake and release of Fe-complexed particles in macrophages.

Xiamen University researchers prepared and characterized Fe-doped carbon nanozyme dots with high peroxidase-like activity, using the food additives ferrous gluconate hydrate and L-aspartic acid as precursors (Qin et al., 2021). Nanozymes are stable artificial enzymes that are able to mimic the structures and functions of natural enzymes. They possess the characteristic modular chemical–physical properties of nanomaterials and at the same time perform catalytic activity similar to those of natural enzymes. The Fe-doped carbon dots (Fe-CDs) were prepared by hydrothermal

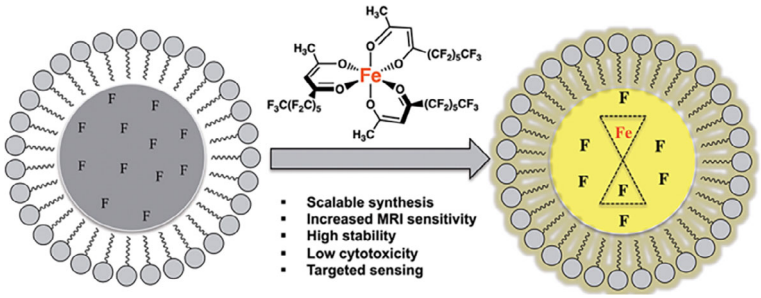

FIGURE 9 Schematic representation of the perfluorocarbon nanoemulsions containing the paramagnetic Fe-PFHA complexes. Reprinted with permission from ACS Applied Bio Materials, 2019, 2, 3836. Copyright 2019 American Chemical Society.

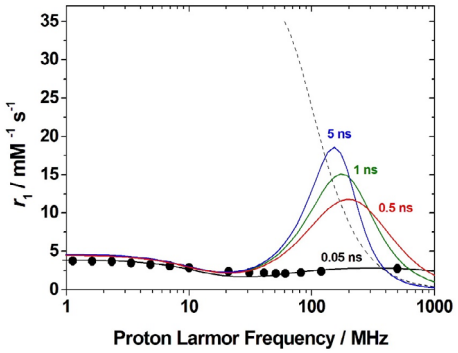

FIGURE 10 Calculated NMRD profiles (1–1000 MHz) showing the effect of increasing τ_R values (0.05–5.0 ns) on the relaxivity of $[Fe(EDTA)(H_2O)]^-$. The experimental data at 298 K (black circles) and the other relaxation parameters are those published (Baranyai et al., 2021). The dotted curve shows the calculated relaxivity, between 60 and 1000 MHz, for the corresponding $[Mn(EDTA)(H_2O)]^-$ complex using the published parameters (Rolla et al., 2013) and a τ_R of 5 ns.

reaction, obtaining uniform nanoparticles with a size around 3.8 nm. The r_1 (0.13 mM^{-1} s^{-1}) and r_2 (9.9 mM^{-1} s^{-1}) relaxivities of Fe-CDs were determined on a 9.4 T MR imaging system, corresponding to an r_2/r_1 ratio of 76.2. Experiments in vitro, in which U87MG cells were incubated with Fe-CD, showed markedly darkened signals compared with the control and precursor groups (glucose-Fe). This data indicates a notable degree of cellular internalization and good intracellular magnetic properties of Fe-CD in T_2-weighted images. In an in vivo MRI experiment, Fe-CDs (20 mg/kg) were intravenously injected into U87MG tumor-bearing mice, and the T_2-MRI signal was monitored on a 9.4 T MRI scanner. As expected, a negative signal intensity in the tumor region was observed, particularly pronounced about 1 h post injection. Therefore, these nanosystems behave as T_2-MRI contrast agent for observation of U87MG tumors.

In recent years, there have been quite a number of studies regarding the use of perfluorocarbon (PFC) based nanoemulsion (NE) probes to tag cells in the intracellular compartment which are then highlighted by ^{19}F MRI (Tirotta et al., 2015). The advantage is the detection in the images of "hot spots" corresponding to the intracellular accumulation of the probes due to the very low quantity of fluorine atoms in the native tissues which results in the absence of a background signal. However, the long relaxation times of ^{19}F represent a well-known obstacle in the development of effective probes. To increase the sensitivity of NEs, the addition or incorporation of paramagnetic metals has proven to be an effective strategy. In particular, flurophilic Fe(III) chelates were proposed and used in some recent studies. In a previous report, E. Ahrens and co-workers conjugated metal-binding β-diketones ("FETRIS") to end groups of a linear perfluoropolyether (PFPE) (Kislukhin et al., 2016). Nanoemulsions based on FETRIS conjugated with PFPE were shown to possess low cytotoxicity (<20%) and good MRI properties. The probe was found to be effective in reducing the ^{19}F T_1 values by about an order of magnitude and this effect is in function of the iron concentration, which can be suitably controlled. More recently, this group synthesized a highly fluorinated ferric *tris*(β-diketonate) chelate based on the use of commercially available (perfluoroheptanoyl)acetone (PFHA) (Figure 9; Wang et al., 2019). Fe-PFHA exhibits high solubility in most common PFCs nanoemulsions and in very nonpolar perfluorohexanes and perfluoromethylcyclohexane.

The Fe-PFHA complex, readily synthesizable in high quantities through a single preparative step, turns out to be highly effective in accelerating ^{19}F relaxation rates (at 9.4 T), even when used in relatively small concentrations. Although in vivo studies have not yet been performed, the cytotoxicity data appear promising.

4 | CONCLUSION

The use of Fe(III) ions as an alternative to Gd(III) in the design of nanosystems for MR imaging is quite recent but a constant growth of this area of research is evident. Several aspects, mostly related to the lower toxicity and the ability to form extremely stable complexes, make this ion preferable to Mn(II), much more explored in the last two decades. Despite the promising and interesting advances highlighted in this review, much remains to be done in the area of Fe(III)-based NPs as T_1 MRI probes. More in-depth in vivo studies are needed, mainly aimed at investigating key issues such as long-term toxicity, biodegradation, elimination mechanisms and biodistribution, since the reported data are still limited.

Moreover, from the results obtained during the studies examined by this review, it is very difficult or almost impossible to assess the real effectiveness of Fe(III)-based nanosystems as a T_1 MRI contrast agent. Unfortunately, in the vast majority of cases the relaxivity values are measured only at one or two frequencies. With a couple of exceptions, a systematic study of the relaxation rates as a function of the applied magnetic field and temperature is lacking. This study is necessary as the knowledge acquired in the case of Gd(III)- and Mn(II)-based systems cannot be of much help in predicting the behavior of Fe(III)-based nanoparticles. Due to the shorter value of the electronic relaxation time of the Fe(III) ions, the relaxivity shows a different dependence on the rotational dynamics and the applied magnetic field B_0. Figure 10 shows the curves describing the magnetic field dependence of r_1 for the $[Fe(EDTA)(H_2O)]^-$ complex and those calculated for increasing values of τ_R (decreasing molecular tumbling). In the molecular tumbling regime typical of NPs (>1 ns) the relaxivity reaches a maximum value between ~2 and 5 T, while it rapidly decreases at higher frequencies. Qualitatively, the behavior of NPs containing Mn(II) and Gd(III) is similar (Caravan et al., 2008), but the r_1 peak is shifted to much lower frequencies (dotted curve in Figure 10).

As a result, at 1.5 T the relaxivity of a Mn(II)-based nanosystem is greater than that of a corresponding Fe(III)-based NP by a factor of at least 5, at 3 T the two nanoprobes have a very comparable efficacy and the one based on Fe(III) has a significantly higher value of r_1 at 7 T.

It is extremely important to measure the values of R_1 (and R_2) at multiple frequencies, preferably between 2 and 5 T, and at multiple temperatures. Of course, whenever possible, it is preferable to measure the magnetic field dependency of r_1 over an extended range of values and at least two temperatures. Data measured in a more systematic way and under well-defined and controlled conditions will allow to achieve a better and more in-depth knowledge of the relationship between the molecular parameters that control the relaxivity and the structural characteristics of the nanoprobes. In turn, this knowledge will allow a rational design of the Fe(III)-containing nanosystems and the full exploitation of their great potential.

In all the studies reported so far, Fe(III) ions are confined inside the nanostructures, where the access of the water solvent molecules is limited and therefore the magnetic interaction with the paramagnetic sites is less effective. This limits the achievable relaxivity by limiting the number of water molecules in (q) or in the vicinity of the inner coordination sphere of Fe(III) and/or by slowing down their exchange rate with the bulk. Thus, nanosystems free from these limitations should be explored, such as those decorated on their surface with stable and inert Fe(III) chelates, preferably with $q = 1$.

Finally, in several systems discussed above the Fe(III) ion is not hydrated ($q = 0$) and therefore the inner sphere relaxation mechanism (IS; $q \geq 1$) is not operative. However, the reported r_1 values are significantly higher than those typical of the outer sphere contribution alone (OS; $q = 0$). This implies the occurrence of a significant contribution due to the water molecules of the second hydration sphere (SS). In fact, the absence of water molecules belonging to the IS of the metal ion does not limit the efficiency of the complexes as $1/T_1$ agents. Given the lack of complete data of r_1 and r_2 as a function of the applied magnetic field and temperature, we can only propose hypotheses to explain the high relaxivity. SS interactions likely arise from dynamic hydrogen bonds between water molecules and polar groups on the nanoparticle proximal to the Fe(III) sites. If the lifetime of these bonds is sufficiently long, the slow molecular tumbling of the NPs represents a factor that enhances relaxivity. Moreover, the presence of exchangeable protons (mainly –OH and $–NH_2$ groups) in the proximity of the metal centres could provide an additional mechanism for relaxivity.

AUTHOR CONTRIBUTIONS

Mauro Botta: Conceptualization (equal); data curation (equal); methodology (equal); writing – original draft (equal); writing – review and editing (equal). **Carlos F. G. C. Geraldes:** Conceptualization (equal); data curation (equal); methodology (equal); writing – original draft (equal); writing – review and editing (equal). **Lorenzo Tei:** Conceptualization (equal); data curation (equal); methodology (equal); writing – original draft (equal); writing – review and editing (equal).

ACKNOWLEDGMENTS

Carlos F. G. C. Geraldes acknowledges the Coimbra Chemistry Center (UID/QUI/00313/2019 and POCI-01-0145-FEDER-027996) of the University of Coimbra. Mauro Botta and Lorenzo Tei acknowledge the financial support of the Ministero dell'Università e della Ricerca (PRIN 2017A2KEPL project).

CONFLICT OF INTEREST

The authors declare no conflict of interest.

DATA AVAILABILITY STATEMENT

Data sharing is not applicable to this article as no new data were created or analyzed in this study.

ORCID

Mauro Botta https://orcid.org/0000-0003-4192-355X
Carlos F. G. C. Geraldes https://orcid.org/0000-0002-0837-8329
Lorenzo Tei https://orcid.org/0000-0002-7027-8396

RELATED WIREs ARTICLES

Functional nanoparticles for magnetic resonance imaging
Integration of gadolinium in nanostructure for contrast enhanced-magnetic resonance imaging
A path toward the clinical translation of nano-based imaging contrast agents
Ultrasmall superparamagnetic iron oxide nanoparticles: A next generation contrast agent for magnetic resonance imaging
Advances of functional nanomaterials for magnetic resonance imaging and biomedical engineering applications

REFERENCES

Ahmad, M., Xu, W., Kim, S. J., Baeck, J. S., Chang, Y., Bae, J. E., Chae, K. S., Park, J. A., Kim, T. J., & Lee, G. H. (2015). Potential dual imaging nanoparticle: Gd_2O_3 nanoparticle. *Scientific Reports*, *5*, 8549. https://doi.org/10.1038/srep08549

Aime, S., Botta, M., Esteban-Gómez, D., & Platas-Iglesias, C. (2019). Characterisation of magnetic resonance imaging (MRI) contrast agents using NMR relaxometry. *Molecular Physics*, *117*(7–8), 898–909. https://doi.org/10.1080/00268976.2018.1516898

Alphandéry, E. (2019). Iron oxide nanoparticles as multimodal imaging tools. *RSC Advances*, *9*(69), 40577–40587. https://doi.org/10.1039/C9RA08612A

An, L., Yan, C., Mu, X., Tao, C., Tian, Q., Lin, J., & Yang, S. (2018). Paclitaxel-induced ultrasmall gallic acid-Fe@BSA self-assembly with enhanced MRI performance and tumor accumulation for cancer theranostics. *ACS Applied Materials and Interfaces*, *10*(34), 28483–28493. https://doi.org/10.1021/acsami.8b10625

Andrews, N. C. (1999). Disorders of iron metabolism. *New England Journal of Medicine*, *341*(26), 1986–1995. https://doi.org/10.1056/NEJM199912233412607

Antwi-Baah, R., Wang, Y., Chen, X., & Yu, K. (2022). Metal-based nanoparticle magnetic resonance imaging contrast Agents: Classifications, issues, and countermeasures toward their clinical translation. *Advanced Materials and Interfaces*, *9*(9), 2101710. https://doi.org/10.1002/admi.202101710

Baranyai, Z., Carniato, F., Nucera, A., Horváth, D., Tei, L., Platas-Iglesias, C., & Botta, M. (2021). Defining the conditions for the development of the emerging class of Fe^{III}-based MRI contrast agents. *Chemical Science*, *12*(33), 11138–11145. https://doi.org/10.1039/D1SC02200H

Bertini, I., Luchinat, C., Parigi, G., & Ravera, E. (2016). *NMR of paramagnetic molecules* (2nd ed.). Elsevier Science.

Botta, M., & Tei, L. (2012). Relaxivity enhancement in macromolecular and nanosized Gd^{III}-based MRI contrast agents. *European Journal of Inorganic Chemistry*, *12*, 1945–1960. https://doi.org/10.1002/ejic.201101305

Caravan, P., Farrar, C. T., Frullano, L., & Uppal, R. (2008). Influence of molecular parameters and increasing magnetic field strength on relaxivity of gadolinium- and manganese-based T1 contrast agents. *Contrast Media and Molecular Imaging*, *4*(2), 89–100. https://doi.org/10.1002/cmmi.267

Das, M. K. (2021). *Multifunctional theranostic nanomedicines in cancer* (1st ed.). Elsevier.

Doane, T. L., & Burda, C. (2012). The unique role of nanoparticles in nanomedicine: Imaging, drug delivery and therapy. *Chemical Society Reviews*, *41*(7), 2885–2911. https://doi.org/10.1039/C2CS15260F

Dong, L., Zhang, P., Lei, P., Song, S., Xu, X., Du, K., Feng, J., & Zhang, H. (2017). PEGylated GdF_3:Fe nanoparticles as multimodal T_1/T_2-weighted MRI and X-ray CT imaging contrast agents. *ACS Applied Materials and Interfaces*, *9*(24), 20426–20434. https://doi.org/10.1021/acsami.7b04438

Gao, Z., Ma, T., Zhao, E., Docter, D., Yang, W., Stauber, R. H., & Gao, M. (2016). Small is smarter: Nano MRI contrast agents—Advantages and recent achievements. *Small*, *12*(5), 556–576. https://doi.org/10.1002/smll.201502309

Geraldes, C. F. G. C., & Laurent, S. (2009). Classification and basic properties of contrast agents for magnetic resonance imaging. *Contrast Media & Molecular Imaging*, *4*, 1–23. https://doi.org/10.1002/cmmi.265

Gianolio, E., Bardini, P., Arena, F., Stefania, R., di Gregorio, E., Iani, R., & Aime, S. (2017). Gadolinium retention in the rat brain: Assessment of the amounts of insoluble gadolinium-containing species and intact gadolinium complexes after repeated administration of gadolinium-based contrast agents. *Radiology*, *285*(3), 839–849. https://doi.org/10.1148/radiol.2017162857

Henderson, L., Neumann, O., Kaffes, C., Zhang, R., Marangoni, V., Ravoori, M. K., Kundra, V., Bankson, J., Nordlander, P., & Halas, N. J. (2018). Routes to potentially safer T_1 magnetic resonance imaging contrast in a compact plasmonic nanoparticle with enhanced fluorescence. *ACS Nano*, *12*(8), 8214–8223. https://doi.org/10.1021/acsnano.8b03368

High, W. A., Ayers, R. A., Chandler, J., Zito, G., & Cowper, S. E. (2007). Gadolinium is detectable within the tissue of patients with nephrogenic systemic fibrosis. *Journal of the American Academy of Dermatology*, *56*(1), 21–26. https://doi.org/10.1016/j.jaad.2006.10.047

Kalinowski, D. S., & Richardson, D. R. (2005). The evolution of iron chelators for the treatment of iron overload disease and cancer. *Pharmacological Reviews*, *57*(4), 547–583. https://doi.org/10.1124/pr.57.4.2

Key, J., & Leary, J. F. (2014). Nanoparticles for multimodal in vivo imaging in nanomedicine. *International Journal of Nanomedicine*, *9*, 711–726. https://doi.org/10.2147/IJN.S53717

Kislukhin, A. A., Xu, H., Adams, S. R., Narsinh, K. H., Tsien, R. Y., & Ahrens, E. T. (2016). Paramagnetic fluorinated nanoemulsions for sensitive cellular fluorine-19 magnetic resonance imaging. *Nature Materials*, *15*(6), 662–668. https://doi.org/10.1038/nmat4585

Koenig, S. H. (1988). Enhancement of contrast in magnetic resonance images by paramagnetic agents: Possibilities and problems. *Israeli Journal of Chemistry*, *28*, 345–353. https://doi.org/10.1002/ijch.198800046

Langereis, S., Geelen, T., Grull, H., Strijkers, G. J., & Nicolay, K. (2013). Paramagnetic liposomes for molecular MRI and MRI-guided drug delivery. *NMR in Biomedicine*, *26*(7), 728–744. https://doi.org/10.1002/nbm.2971

Laurent, S., Forge, D., Port, M., Roch, A., Robic, C., Vander Elst, L., & Muller, R. N. (2008). Magnetic iron oxide nanoparticles: Synthesis, stabilization, vectorization, physicochemical characterizations, and biological applications. *Chemical Reviews*, *108*(6), 2064–2110. https://doi.org/10.1021/cr068445e

Lee, H., Hoang, B., Fonge, H., Reilly, R. M., & Allen, C. (2010). In vivo distribution of polymeric nanoparticles at the whole-body, tumor, and cellular levels. *Pharmaceutical Research*, *27*(11), 2343–2355. https://doi.org/10.1007/s11095-010-0068-z

Li, X., Lovell, J. F., Yoon, J., & Chen, X. (2020). Clinical development and potential of photothermal and photodynamic therapies for cancer. *Nature Reviews Clinical Oncology*, *17*(11), 657–674. https://doi.org/10.1038/s41571-020-0410-2

Li, Y., Huang, Y., Wang, Z., Carniato, F., Xie, Y., Patterson, J. P., Thompson, M. P., Andolina, C. M., Ditri, T. B., Millstone, J. E., Figueroa, J. S., Rinehart, J. D., Scadeng, M., Botta, M., & Gianneschi, N. C. (2016a). Polycatechol nanoparticle MRI contrast Agents. *Small*, *12*(5), 668–677. https://doi.org/10.1002/smll.201502754

Li, Y., Xie, Y., Wang, Z., Zang, N., Carniato, F., Huang, Y., Andolina, C. M., Parent, L. R., Ditri, T. B., Walter, E. D., Botta, M., Rinehart, J. D., & Gianneschi, N. C. (2016b). Structure and function of iron-loaded synthetic melanin. *ACS Nano*, *10*(11), 10186–10194. https://doi.org/10.1021/acsnano.6b05502

Liu, F., He, X., Chen, H., Zhang, J., Zhang, H., & Wang, Z. (2015). Gram-scale synthesis of coordination polymer nanodots with renal clearance properties for cancer theranostic applications. *Nature Communications*, *6*, 8803. https://doi.org/10.1038/ncomms9003

Marasini, R., Rayamajhi, S., Moreno-Sanchez, A., & Aryal, S. (2021). Iron(III) chelated paramagnetic polymeric nanoparticle formulation as a next-generation T_1-weighted MRI contrast agent. *RSC Advances*, *11*(51), 32216–32226. https://doi.org/10.1039/d1ra05544e

Marcus, Y. (1988). Ionic radii in aqueous solutions. *Chemical Reviews*, *88*(8), 1475–1498. https://doi.org/10.1021/cr00090a003

Mi, P., Kokuryo, D., Cabral, H., Wu, H., Terada, Y., Saga, T., Aoki, I., Nishiyama, N., & Kataoka, K. (2016). A pH-activatable nanoparticle with signal-amplification capabilities for non-invasive imaging of tumour malignancy. *Nature Nanotechnology*, *11*(8), 724–730. https://doi.org/10.1038/nnano.2016.72

Miao, Y., Xie, F., Cen, J., Zhou, F., Tao, X., Luo, J., Han, G., Kong, X., Yang, X., Sun, J., & Ling, J. (2018). Fe^{3+}@polyDOPA-b-polysarcosine, a T_1-weighted MRI contrast agent via controlled NTA polymerization. *ACS Macro Letters*, *7*(6), 693–698. https://doi.org/10.1021/acsmacrolett.8b00287

Mu, X., Yan, C., Tian, Q., Lin, J., & Yang, S. (2017). BSA-assisted synthesis of ultrasmall gallic acid–Fe(III) coordination polymer nanoparticles for cancer theranostics. *International Journal of Nanomedicine*, *12*, 7207–7223. https://doi.org/10.2147/IJN.S146064

Patel, A., Asik, D., Snyder, E. M., Dilillo, A. E., Cullen, P. J., & Morrow, J. R. (2020). Binding and release of Fe^{III} complexes from glucan particles for the delivery of T_1 MRI contrast agents. *ChemMedChem*, *15*(12), 1050–1057. https://doi.org/10.1002/cmdc.202000003

Patra, D., Kumar, P., Samanta, T., Chakraborty, I., & Shunmugam, R. (2022). Coordinately tethered iron(III) fluorescent nanotheranostic polymer ascertaining cancer cell mitochondria destined potential chemotherapy and T1-weighted MRI competency. *ACS Applied Bio Materials*, *5*(3), 1284–1296. https://doi.org/10.1021/acsabm.1c01300

Peters, J. A. (2020). Relaxivity of manganese ferrite nanoparticles. *Progress in Nuclear Magnetic Resonance Spectroscopy*, *120–121*, 72–94. https://doi.org/10.1016/j.pnmrs.2020.07.002

Phatruengdet, T., Intakhad, J., Tapunya, M., Chariyakornkul, A., Hlaing, C. B., Wongpoomchai, R., & Pilapong, C. (2020). MRI contrast enhancement of liver pre-neoplasia using iron–tannic nanoparticles. *RSC Advances*, *10*(58), 35419–35425. https://doi.org/10.1039/d0ra07308c

Phatruengdet, T., Khuemjun, P., Intakhad, J., Krunchanuchat, S., Chariyakornkul, A., Wongpoomchai, R., & Pilapong, C. (2022). Pharmacokinetic/pharmacodynamic determinations of iron-tannic molecular nanoparticles with its implication in MR imaging and enhancement of liver clearance. *Nano*, *6*(2), 195–204. https://doi.org/10.7150/ntno.63310

Qin, J., Liang, G., Feng, Y., Feng, B., Wang, G., Wu, N., Zhao, Y., & Wei, J. (2020). Synthesis of gadolinium/iron–bimetal–phenolic coordination polymer nanoparticles for theranostic applications. *Nanoscale*, *12*(10), 6096–6103. https://doi.org/10.1039/c9nr10020b

Qin, R., Feng, Y., Ding, D., Chen, L., Li, S., Deng, H., Chen, S., Han, Z., Sun, W., & Chen, H. (2021). Fe-coordinated carbon nanozyme dots as peroxidase-like nanozymes and magnetic resonance imaging contrast agents. *ACS Applied Bio Materials*, *4*(7), 5520–5528. https://doi.org/10.1021/acsabm.1c00336

Raymond, K. N., Allred, B. E., & Sia, A. K. (2015). Coordination chemistry of microbial iron transport. *Accounts of Chemical Research*, *48*(9), 2496–2505. https://doi.org/10.1021/acs.accounts.5b00301

Reynders, H., Van Zundert, I., Silva, R., Carlier, B., Deschaume, O., Bartic, C., Rocha, S., Basov, S., Van Bael, M. J., Himmelreich, U., Verbiest, T., & Zamora, A. (2021). Label-free iron oxide nanoparticles as multimodal contrast agents in cells using multi-photon and magnetic resonance imaging. *International Journal of Nanomedicine*, *16*, 8375–8389. https://doi.org/10.2147/IJN.S334482

Rolla, G. A., Platas-Iglesias, C., Botta, M., Tei, L., & Helm, L. (2013). ^{1}H and ^{17}O NMR relaxometric and computational study on macrocyclic Mn(II) complexes. *Inorganic Chemistry*, *52*(6), 3268–3279. https://doi.org/10.1021/ic302785m

Shander, A., Cappellini, M. D., & Goodnough, L. T. (2009). Iron overload and toxicity: The hidden risk of multiple blood transfusions. *Vox Sanguinis*, *97*(3), 185–197. https://doi.org/10.1111/j.1423-0410.2009.01207.x

Smith, B. R., & Gambhir, S. S. (2017). Nanomaterials for in vivo imaging. *Chemical Reviews*, *117*(3), 901–986. https://doi.org/10.1021/acs.chemrev.6b00073

Snyder, E. M., Asik, D., Abozeid, S. M., Burgio, A., Bateman, G., Turowski, S. G., Spernyak, J. A., & Morrow, J. R. (2020). A class of Fe^{III} macrocyclic complexes with alcohol donor groups as effective T_1 MRI contrast agents. *Angewandte Chemie International Edition*, *59*(6), 2435–2440. https://doi.org/10.1002/anie.201912273

Starmans, L. W. E., Hummelink, M. A. P. M., Rossin, R., Kneepkens, E. C. M., Lamerichs, R., Donato, K., Nicolay, K., & Grüll, H. (2015). ^{89}Zr- and Fe-labeled polymeric micelles for dual modality PET and T_1-weighted MR imaging. *Advanced Healthcare Materials*, *4*(14), 2137–2145. https://doi.org/10.1002/adhm.201500414

Tirotta, I., Dichiarante, V., Pigliacelli, C., Cavallo, G., Terraneo, G., Bombelli, F. B., Metrangolo, P., & Resnati, G. (2015). ^{19}F magnetic resonance imaging (MRI): From design of materials to clinical applications. *Chemical Reviews*, *115*(2), 1106–1129. https://doi.org/10.1021/cr500286d

Vander Elst, L., Roch, A., Gillis, P., Laurent, S., Botteman, F., Bulte, J. W. M., & Muller, R. N. (2002). Dy-DTPA derivatives as relaxation agents for very high field MRI: The beneficial effect of slow water exchange on the transverse relaxivities. *Magnetic Resonance in Medicine*, *47*(6), 1121–1130. https://doi.org/10.1002/mrm.10163

Villaraza, A. J. L., Bumb, A., & Brechbiel, M. W. (2010). Macromolecules, dendrimers, and nanomaterials in magnetic resonance imaging: The interplay between size, function, and pharmacokinetics. *Chemical Reviews*, *110*(5), 2921–2959. https://doi.org/10.1021/cr900232t

Wahsner, J., Gale, E. M., Rodriguez-Rodriguez, A., & Caravan, P. (2019). Chemistry of MRI contrast agents: Current challenges and new frontiers. *Chemical Reviews*, *119*(2), 957–1057. https://doi.org/10.1021/acs.chemrev.8b00363

Wang, C., Adams, S. R., Xu, H., Zhu, W., & Ahrens, E. T. (2019). β-Diketonate-iron(III) complex: A versatile fluorine-19 MRI signal enhancement agent. *ACS Applied Bio Materials*, *2*(9), 3836–3842. https://doi.org/10.1021/acsabm.9b00455

Whittaker, P., Ali, S. F., Imam, S. Z., & Dunkel, V. C. (2002). Acute toxicity of carbonyl iron and sodium iron EDTA compared with ferrous sulfate in young rats. *Regulatory Toxicology and Pharmacology*, *36*(3), 280–286. https://doi.org/10.1006/rtph.2002.1577

Williams, M. W., Hoeschele, J. D., Turner, J. E., Jacobson, K. B., Christie, N. T., Paton, C. L., Smith, L. H., Witschi, H. R., & Lee, E. H. (1982). Chemical softness and acute metal toxicity in mice and Drosophila. *Toxicology and Applied Pharmacology*, *63*(3), 461–469. https://doi.org/10.1016/0041-008X(82)90274-5

Xue, X., Bo, R., Qu, H., Jia, B., Xiao, W., Yuan, Y., Vapniarsky, N., Lindstrom, A., Wu, H., Zhang, D., Li, L., Ricci, M., Ma, Z., Zhu, Z., Lin, T., Louie, A. L., & Li, Y. (2020). A nephrotoxicity-free, iron-based contrast agent for magnetic resonance imaging of tumors. *Biomaterials*, *257*, 120234–120245. https://doi.org/10.1016/j.biomaterials.2020.120234

Yu, Y., Gutierrez, E., Kovacevic, Z., Saletta, F., Obeidy, P., Suryo Rahmanto, Y., & Richardson, D. R. (2012). Iron chelators for the treatment of cancer. *Current Medicinal Chemistry*, *19*(17), 2689–2702. https://doi.org/10.2174/092986712800609706

How to cite this article: Botta, M., Geraldes, C. F. G. C., & Tei, L. (2022). High spin Fe(III)-doped nanostructures as T_1 MR imaging probes. *WIREs Nanomedicine and Nanobiotechnology*, e1858. https://doi.org/10.1002/wnan.1858